# Adsorption of the Cationic Surfactant Benzyldimethylhexadecylammonium Chloride at the Silica−Water Interface and Metal Salt Effects on the Adsorption Kinetics

Zlata Grenoble and Steven Baldelli*

Department of Chemistry, University of Houston, 4800 Calhoun Rd., Houston, Texas 77004-5003, United States

Ⓢ *Supporting Information*

ABSTRACT: The adsorption of the cationic surfactant benzyldimethylhexadecylammonium (BDMHA$^+$) chloride has been studied at the hydrophilic silica−water interface by Raman spectroscopy in total internal reflection geometry (TIR Raman). This Raman spectroscopic technique takes advantage of an evanescent electric field that is generated at the silica−water interface in TIR mode with specific probing depth. The present study demonstrates the capabilities of the TIR Raman sampling configuration to provide structural information and simultaneously serve as an experimental platform for studying thermodynamic and kinetic properties of BDMHA$^+$Cl$^-$ at the silica−water interface at neutral pH and compare its adsorption behavior with the modified adsorption properties in the presence of four different concentrations of a divalent metal salt. Spectral analysis of the Raman scattering intensities as a function of time and concentration provided the input data for evaluating adsorption properties of the surfactant in the absence and presence of the metal salt additive. Addition of the magnesium metal salt lowered the cmc, altered the surface excess of the surfactant, and increased the Langmuir adsorption constants, as well as the magnitude of the free energy of adsorption, and adsorption kinetics, proportional to the concentrations of the metal salt. Adsorption isotherms based on a modified Langmuir adsorption model were established for five systems: the pure surfactant in aqueous solution, and the surfactant in the presence of 5, 10, 50, and 100 mM of magnesium chloride. The metal salt did not enhance surfactant adsorption at very low surfactant concentrations below 5 μM, where adsorption occurs by electrostatic attraction; the divalent metal salt, however, favorably influenced the adsorption behavior in the aggregate formation region by reducing the electrostatic repulsion between the polar surfactant head groups, and enhancing the hydrophobic effect between the hydrophobic surfactant alkyl chains and the polar water molecules.
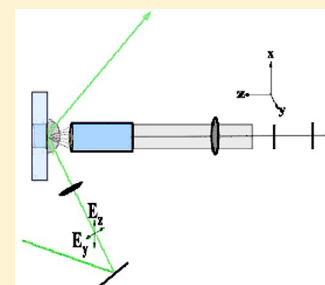
INTRODUCTION

Cationic surface active agents (surfactants) are used in numerous applications as dispersants, surface tension modifiers, and cleaning detergents, and in industrial processes, also as additives in corrosion inhibitors. They are known for their adsorption-enhancing and interfacial modulating properties at the solid−liquid interface in oil recovery processes.[1−4] Cationic surfactants typically consist of a hydrophobic alkyl chain, containing between 12 and 18 carbon atoms, and a positively charged hydrophilic head group. The head groups that are frequently encountered are based on the highly water-soluble and polar trimethylammonium cation, or may contain a modified ammonium head group with a substituted methyl ligand, i.e., benzyldimethylammonium.[5−8]

The search for improved surfactant performance gives strong incentives to study the effects of different head-group configurations on the surfactants' interfacial properties, one of them being the substitution of a methyl group by a benzyl ligand at the cationic ammonium head group. This ligand type alters the physicochemical properties of a surfactant as compared to other trialkyl homologues.[5,6,9,10] Cationic surfactants of this type are employed in oil exploration, oil well drilling, and completion, primarily in 2° and 3° oil recovery processes[11−15] where they also act as dispersants, and emulsion breakers; they are frequently used as constituents in binary surfactant mixtures to modulate oil-wetting or water-wetting interfacial properties,[16] as well as control the adsorption to certain soil and rock formations.[2,17−19] One significant area of application is corrosion inhibition in oil well drilling and completion operations, due to their effectiveness in reducing corrosion rates of steel equipment, when paired with the appropriate corrosion inhibition enhancement additive.[12,14]

One key concern in surfactant formulation is to keep the surfactant concentration at minimum levels to lower production and maintenance costs,[20] and comply with environmental regulations, by choosing the best suitable surfactant and by mixing additives into the surfactant matrix.[21,20] Since quartz or silica is a major constituent of soil formations, adsorption specifically to quartz and related thermodynamic and kinetic properties of one representative surfactant, containing a benzyl group ligand at the ammonium head and a C$_{16}$ alkyl chain, were evaluated in this study.[11,22−25]

The relevant parameters for predicting adsorption behavior, in particular, the adsorption isotherm at the silica−water

interface, the concentrations that correspond to the critical micelle concentration (cmc), have been determined for the pure surfactant and also for the surfactant in the presence of varying concentrations of a divalent metal salt.[1,26] The benzyldimethylhexadecylammonium chloride (BDMHA$^+$) adsorption isotherms for the various systems that were established from TIR Raman analysis follow a Langmuir or a modified Langmuir adsorption model that includes an additional energy parameter to account for the lateral interaction energy between neighboring molecules.[27]

TIR Raman spectroscopy is suitable for probing the silica−water interface, since the Raman scattering from water molecules is low, as compared to IR, and the probed C−H vibrational modes exhibit strong Raman scattering cross sections. Examples are the study of biological systems, i.e., plant cell membranes,[28] phospholipid membranes at solid silica interfaces,[29] and monolayers of organic mixtures, confined and pressurized between solid layers.[30,31] Variation of the sampling geometry allows control over penetration depths within a specific nanometer range and surface selectivity as demonstrated with the analysis of polymer films.[32,33]

Raman spectroscopy in total internal reflection (TIR) geometry provides a platform for direct measurement of the adsorbed species at the silica−water interface[34,35] by correlating the Raman scattering intensity to the surface excess of the pure compound, and the enhanced surfactant adsorption with magnesium chloride as an additive. The Raman scattering signals were used as input to develop an adsorption isotherm model, for both the pure compound and the surfactant−metal chloride mixtures, and simultaneously providing spectroscopic information.[36]

At low surfactant concentrations, benzyldimethylhexadecylammonium chloride (Figure 1) adsorption is initiated by
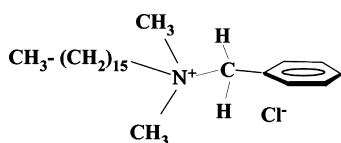
Figure 1. Molecular structure of benzyldimethylhexadecylammonium chloride (BDMHA$^+$Cl$^-$).

electrostatically driven mechanisms. At higher concentrations, and after surface charge neutralization, the prevailing adsorption mechanism in the hemimicelle formation or aggregate forming region is hydrophobic effects arising from the interaction between the nonpolar alkyl chain of the surfactant and the surrounding water molecules.[1,10,37] Two competing processes of Gibbs free energy lowering by micellization versus energy lowering by adsorption to the surface occur simultaneously in the silica−water−surfactant system, controlled by the interfacial properties and the surfactant−solvent interaction,[2,38] with noticeably slow kinetics of adsorption to silica in the region of surfactant aggregate formation.

The second part of this study relates to surfactant adsorption enhancement induced by a metal salt additive, i.e., the divalent metal salt magnesium chloride. Divalent metal salts have previously been studied in combination with anionic compounds where specific adsorption of the positively charged metal ions at favorable conditions induced charge inversion at the silica surface and promoted the adsorption of negatively charged species at the silica−water interface.[25] The goal of this

study was, however, to identify the effects of metal halide salt addition on the surfactant−solution−silica surface interaction due to change of solvent polarity and ionic strength, as well as screening of the head-group charges by the added counterions,[38] and their effect on surfactant adsorption behavior at the silica−water interface.

■ BACKGROUND AND THEORY

Surface Tension Measurement and Critical Micelle Concentration. Surface tension measurements of benzyldimethylhexadecylammonium chloride (Figure 1) were carried out using the "du Nouy" ring method (Kruess tensiometer, Kruess GmbH, Germany). The surface tension measurements provided an estimate of the cmc parameter in comparison to the cmc value from the adsorption isotherm, and to literature values.[39−41] Measurements before and after purification by recrystallization from acetone−methanol (90/10 v/v) of the purchased compound served as indicator of the purity of the surfactant.

The cmc of a surfactant is determined by the nature of the hydrophilic head group, the length of the hydrophobic alkyl chain, and additional functional groups that may be part of the hydrophobic tail or head group; the cmc of a given ionic surfactant decreases with each methylene group that is added to its hydrophobic alkyl tail as a result of decreasing free energy of micellization $(-G_{mic})$ by transfer of additional methylene groups from the aqueous phase to the interior portion of the aggregate.[38] The nature of the cationic head group, and the charge-screening capabilities of the counterion, in general a halide like chloride or bromide, further influence the aggregation and adsorption of the surfactant.[1,10,19,26] The chloride anion with lower affinity to the positively charged head group is considered less effective in screening the head-group charge as compared to the larger bromide anion, resulting in lower surfactant aggregation numbers.[9,10]

The cmc for pure BDMHA$^+$Cl$^-$ was estimated from surface tension curve fitting and applying the thermodynamic relationship as shown in eq 1.

$$\Gamma_{max} = -\frac{1}{2RT}\left(\frac{d\gamma}{d \ln[C]}\right) \tag{1}$$

where Γ_{max} defines the maximum surface coverage, γ refers to the surface tension, and $[C]$ determines the surfactant concentration. The thermodynamic and kinetic aspects of the surfactant adsorption at the silica−water interface were deduced from the signal intensities measured by Raman spectroscopy in TIR geometry.

Addition of electrolytes is known to affect the ionic strength of the aqueous phase and thus the aggregation behavior of the surfactant in solution, resulting in either surface excess enhancing[42] or lowering effects.[43] One goal of this study was to evaluate the effects of a common, divalent metal salt on the adsorption thermodynamics and kinetics of the particular surfactant under investigation, and determine optimum application conditions for this type of surfactant.

Total internal reflection (TIR) Raman spectroscopy combines the analytical capabilities of Raman spectroscopy with the advantages of total internal reflection mode where the sample is not directly exposed to a highly energetic laser beam that might cause damage of the material under study.[34,35] The evanescent electric field that is generated at the silica−water interface contains sufficient excitation energy for Raman

scattering, but its energy flux in the z-direction, perpendicular to the interface, is practically nonexistent based on the Poynting vector description.[44] The incident excitation beam, which can be either p- or s-polarized, is totally internally reflected when the incident angle θ_i is equal to or larger than the critical angle, and the medium of incidence, here the fused silica, has a higher index of refraction than the medium of the transmitted beam (following Snell's law).

The critical angle is given by $\theta_c = \sin^{-1}(n_t/n_i)$,[35,44] where n stands for the refractive index (also defined as the square root of the dielectric constant at optical frequencies) of the respective medium[45] and the subscripts i and t refer to the incident and transmitted medium. The critical angle was determined as 65.6° for the silica−water system used in this study, and an evanescent field penetration depth of approximately 100 nm for the refractive index ratio of 1.33/1.46 and an incident laser wavelength of 532 nm. The resulting electric field enhancement as function of the Fresnel transmission coefficient is proportional to the square of the ratio of the transmitted versus the incident electric field. Its derivation from the complex electric field propagation vectors is described in more detail in the Supporting Information.

It follows from the Fresnel transmission coefficients and electric field vector description that the evanescent wave penetration depth into the medium of lower refractive index becomes smaller with larger incident angle θ_i relative to the critical angle as shown by eq 2; the electric field enhancement increases exponentially with decreasing angle of incidence and can be up to several times the original electric field.[44]

$$z = d = \frac{1}{\beta} = \frac{\lambda_0}{4\pi(n_i^2 \sin^2 \theta_i - n_t^2)^{1/2}} \tag{2}$$

The energy density of the focused laser beam can be varied by choosing the respective laser beam expansion and focusing optics to define the focused laser spot size on the sample. In this study, the incident angle of the excitation beam was set at 73° giving a narrow beam diameter, with a small numerical aperture (N.A.) of 0.11, at the focusing point. The polarization of the excitation laser source was chosen as s-polarized light in all experiments related to the adsorption isotherms, since the signal scattering intensity from s-polarized incident light proved to be stronger in TIR sampling and light collection geometry as compared to the signal intensity in p-polarized sampling geometry. The symmetric or diagonal elements of the derived Raman polarizability tensor of surface molecules interact strongly with the incoming E_y electric field vector from s-polarized incident light that probes predominantly the diagonal (symmetric) elements of the derived Raman polarizability tensor, α'_{yy}, relative to the surface, as compared to the off-diagonal derived Raman polarizability tensors that are most sensitive to p-polarized incident light, with the electric field vector perpendicular to the surface plane.

The electric field enhancement is strongest for p-polarized light versus s-polarized incident light at and close to the critical angle, based on the Fresnel transmission coefficient definition, but the Fresnel transmission coefficient at the incident angle of 73° is similar in magnitude for both p- and s-polarized incident light and the sampling geometry with s-polarized incident light gives stronger Raman scattering signals in TIR sampling configuration, in particular of the symmetric vibrational modes.[36] Adsorption isotherms of the surfactant could be determined with a detection limit (S/N) of 3 counts s^{-1},

corresponding to 1 μM of the pure surfactant concentration and 0.014 fractional coverage; the signal intensity ratios of Raman scattering in both p- and s-sampling geometry from additional experiments were used on a qualitative basis for orientational analysis and tentative prediction of the most likely structures of the aggregates present at the interface.

A description of the experimental TIR Raman layout is presented in the following Experimental Section followed by a detailed discussion of the experimental results obtained from the analysis of the adsorption behavior of the studied surfactant.

Adsorption isotherms were determined for all five systems studied: the pure surfactant, and the surfactant with addition of 5, 10, 50, and 100 mM of magnesium chloride; the relevant adsorption parameters could be extracted from the Raman scattered signals of the relevant C−H stretching vibrations observed in the high-frequency region of the Raman spectra (Figure 3, Table 1); the adsorption process was modeled as a

Table 1. Raman Peak Assignment[35,56−58]

cm^{-1}	vibrational mode	relative intensity
2718	C−H ν_δ bend overtone	weak
2789	C−H ring comb. band	weak
2852	CH$_2$ ν_s	strong
2872	CH$_3$ ν_s	very weak, not shown in fitted spectrum
2889	CH$_2$ ν_{as}	strong
2927	CH$_2$ ν_{sFR}	weak
2965	CH$_3$ ν_{as}	weak
2980	N−CH$_3$ ν_s	weak
3040	N−CH$_3$ ν_{as}	weak
3064	C−H ring ν_s	medium

Langmuir and modified Langmuir isotherm, also referred to in the literature as the Frumkin−Fowler−Guggenheim model, where the interaction energy between neighboring molecules is taken into account, and the adsorption constant $K(\theta)$ also depends on an additional energy parameter arising from lateral interaction and the fractional surface coverage.[46,47] These models were used as a basis to determine the equilibrium adsorption constants, change in Gibbs free energy of adsorption, and the interaction energy parameter (Table 2) according the following expressions:

$$\frac{\theta}{(1-\theta)} = K_{mod}[C] \tag{3}$$

$$K_{mod} = K_L e^{g\theta} \tag{4}$$

and

$$g = nE/RT \tag{5}$$

where K_L and K_{mod} define the Langmuir and modified Langmuir constant, θ represents the fractional coverage, and the constant g is introduced for $g = nE/RT$ that includes the number of neighboring molecules n and the interaction energy E.[27,48] A normalized surface coverage has been used in this study by setting the coverage at the cmc of the pure surfactant equal to unity.

Divalent metals have shown affinity toward silica surfaces under certain favorable conditions with silica surface binding rates and energies of adsorption that depend on the concentrations of the background electrolytes,[49,50] their potential effects on the intrinsic surface charge, and interaction with the silica surface silanols.[50−52]

Addition of magnesium chloride to the water−surfactant system, near neutral pH, in this study, appeared to result in surface charge neutralization due to magnesium ions adsorbing at the surface, as indicated by attenuation of the electrostatic attraction of the surfactant with electrolyte addition in the low surfactant concentration regime, and discussed in the Results section of this paper. Negative surface charge buildup via displacement of the silanol protons, as shown in studies of divalent metal adsorption at the silica−water interface,[51] is inconsistent with the results of this work. After initially decreasing the surface coverage relative to the pure surfactant, the metal salt enhanced BDMHA[+] adsorption kinetics and increased the maximum surface coverage, relative to the lowest electrolyte concentration, and proportional to increasing metal salt concentrations, by enhancing the so-called hydrophobic effect (Figure 13). First, increased ionic strength of the aqueous phase promotes adsorption of surfactant to the solid−water interface. Second, the counterions from the added electrolyte screen the head-group charges and allow for a higher and more effective aggregation of surfactant monomers with increasing aggregation number and increase of the micellar packing parameter of the surfactant in solution.[38]

■ EXPERIMENTAL SECTION

Surface tension measurements ("du Nouy" ring method (ring tensiometer, Kruess GmbH, Hamburg, Germany) of benzyldimethylhexadecylammonium chloride (Sigma-Aldrich, purity >97%) before and after purification by recrystallization (three times) from acetone−methanol (90/10 v/v) were made to obtain the surface tension curve for the relevant concentration range with a cmc value of 0.49 mM from curve fitting and applying the thermodynamic relationship for the pure surfactant as shown in eq 1.

The in-house-built TIR Raman spectroscopy setup has capabilities for both Raman spectral analysis in conventional and in total internal reflection (TIR) Raman mode (Figure 2).
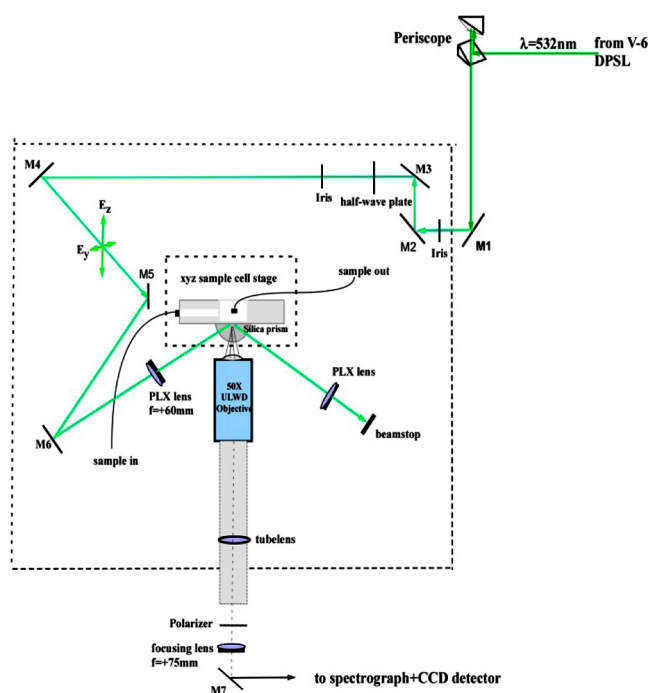

Figure 2. Experimental design and layout of TIR Raman system.

The laser source is a diode-pumped, solid-state laser with 532 nm emission wavelength, beam radius of 2.25 mm at the laser beam output, and several watts output power (Verdi-6, Coherent Inc.). The output power of the diode laser was set at 0.5 W for the adsorption isotherm studies, with acquisition times of 10 min. The resulting numerical aperture (N.A.) was determined as 0.11 at the focusing optics, with a resulting elliptical spot size of approximately 200 μm^2 (4.3 × 14.7 μm^2) focused on the sample, and a maximum power density of 220 kW cm^{-2}. Setting the incident angle farther away from the critical angle provides sufficient energy density on the sample while maintaining the probing depth at around 100 nm with more surface specific information of the molecules in both quantitative terms, i.e., surface excess, and molecular identify, at the interface,[34−36] and only negligible signal contribution from molecules in the bulk at surfactant concentrations below or around the cmc.

The circular sampling cell was constructed from Teflon material with an internal diameter of 14.5 mm and a width of 8.5 mm to give a cell volume of 1.23 cm^3. It contains the TIR hemisphere (ISP Optics) with the flat surface in vertical position, perpendicular to the experimental surface. The hemispherical 1 in. diameter IR grade fused silica prism serves a dual function, as the TIR element itself, and simultaneously as the silica solid surface. The aqueous solutions containing the respective surfactant concentrations in ultrapure water (Millipore 18.2 MΩ) were introduced into the sample cell via 1.5 mm i.d. PTFE lines connected to a peristaltic pump (Lab-line Peristaltic Inducer) for Raman spectral analysis at stagnation point flow conditions (Figure 2).

The Raman signal collection optics consist of a 50× ULWD objective (Mitutoyo, 0.55 N.A., 17 mm working distance) attached at the front of a 250 mm long lens tube, and a 1 in. diameter biconvex focusing lens (f = 200 mm), located approximately 230 mm behind the collection objective in the 1 in. diameter lens tube compartment for collimation of the incoming Raman scattered signals. The collected photons are focused into the spectrograph by a second focusing lens (f = 75 mm). The spectrograph itself contains two pairs of focusing optics. The first pair is located right behind the spectrograph entrance with f = 50 mm, with a laser line rejection filter for excluding the Rayleigh line of 532 nm. The focused signal is sent through an entrance slit of 100 μm slit width and a second pair of focusing optics with f = 85 mm (Kaiser Optical, 1.8 fi) onto a high-frequency transmission grating with 2600 grooves/mm and 3.5 nm mm^{-1} reciprocal resolution (Kaiser Optical Instruments) and is detected by a back illuminated charge-coupled device (DU-420A BR-DD, 26.6 μm pixel^{-1}, Andor Technology).

The effective spectral range of the spectrograph and high-frequency grating extends from 2250 to 4350 cm^{-1} (for analysis of mid- and high-frequency vibrational modes). Spectral acquisition times were kept at a total of 10 min (10 × 60 s exposure times added together) throughout the experiment. Background correction for the intrinsic signal contribution from the silica and the water in the bulk was carried out by introducing ultrapure water into the sample cell and acquiring the background signal with Raman scattering from silica and water only, using identical acquisition parameters and sampling geometries as with the subsequent analytical samples, and subtracting it from the subsequent Raman spectra of the aqueous solutions containing the compounds of interest and converting to counts s^{-1}, using the background correction

262

dx.doi.org/10.1021/jp3091107 | J. Phys. Chem. B 2013, 117, 259−272

algorithm provided with the data acquisition software (Solis ver. 4.16.3). Data acquisition was in multitrack mode (which corresponds to spectroscopy mode), at 1.6× preamplifier gain, and 64.25 μs vertical pixel shift speed with an effective resolution of approximately 5 cm^{-1}. The raw background-corrected Raman spectral data were further processed with the Origin Ver. 7.0 spectral analysis software to correct for laser and baseline drifts; the resulting spectra provided the input for developing the adsorption isotherms, interpretation of surfactant thermodynamic and kinetic properties, and structural analysis.

The adsorption isotherms of the pure surfactant, as well as surfactant with metal salt addition, are based on the symmetric vibrational mode of the methylene stretch in the alkyl chains at 2852 cm^{-1}, which was superior in terms of reproducibility as compared to those based on the integrated area over the C−H stretching region (Figure 3). Although other Raman vibrational
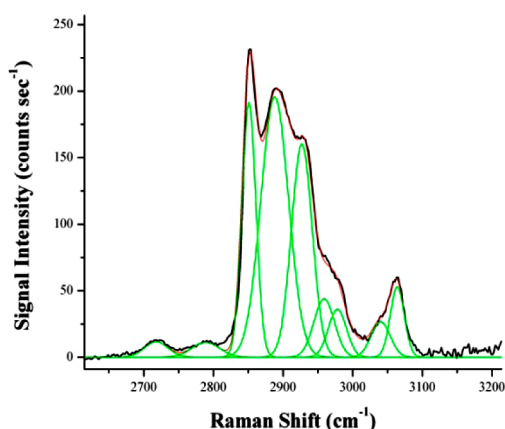

Figure 3. Raman spectrum of the C−H stretching region in s-polarized mode for BDMHA$^+$ fitted to a Gaussian model.

modes, i.e., the benzyl C−H vibration at 3064 cm^{-1}, are clearly visible and reproducible in the collected Raman spectra, the symmetric methylene stretching mode provides the highest signal intensity at 3 counts s^{-1} detection limit (Figures 6 and 7). Figure 3 shows the fitted Raman spectrum obtained with s-polarized incident laser excitation from a 0.5 mM surfactant concentration in the C−H stretching region with peak assignments of the C−H stretching region summarized in Table 1. Figure 4 presents the same surfactant at a concentration of 0.4 mM in p-polarized geometry for comparison. All isotherms were fitted to a Langmuir or modified Langmuir adsorption model (eq 3) after normalizing the signal intensity and setting the surface coverage at the cmc equal to one.

■ RESULTS AND DISCUSSION

The surface tension of BDMHA$^+$Cl$^-$ (Figure 1) was determined for the compound as purchased, before purification, and also after purification by recrystallization to remove impurities noticeable as a depression or second minimum at a concentration of 0.40 mM in the isotherm of the unpurified compound.[3,15,23] Surface tension data showed a minimum value of 35.5 mN m^{-1} at the cmc of 0.49 mM that was used only as a reference value for comparison with the adsorption isotherm data from this study and literature data. This cmc value is slightly higher than some values reported in literature, i.e., 0.34[53] and 0.40 mM,[39] but it agrees well with the cmc obtained
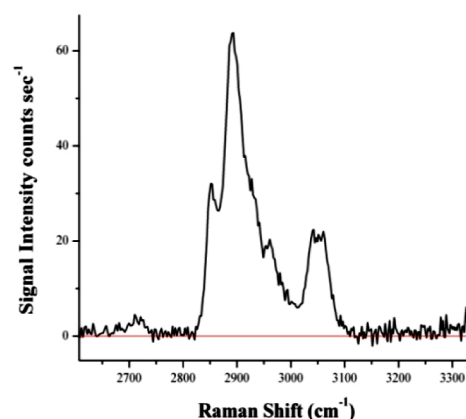

Figure 4. Raman spectrum of the same C−H region in p-polarized sampling geometry.

from adsorption isotherms and other literature data that reported almost identical values of 0.485[54] and 0.49 mM.[55]

A representative Raman spectrum was obtained from the 0.5 mM surfactant concentration—which approximates the cmc concentration—and fitted to a Gaussian model that shows the prominent Raman vibrational modes in the C−H stretching region (Figure 3). The spectral acquisition of the scattering intensity from s-polarized incident light from the 532 nm laser line was carried out without any polarizer in the collection optics; peak assignments for the respective Raman vibrational modes are summarized in Table 1. A Raman spectrum corresponding to a surfactant concentration of 0.4 mM in p-polarized incident laser beam geometry is shown for comparison of both the overall signal intensity decrease and the signal intensity ratio change of the symmetric methylene vibrational modes versus their antisymmetric stretching modes (Figure 4). The stronger interaction of off-diagonal, antisymmetric Raman tensor modes with the incident vertically polarized electric field is shown by the increase of the antisymmetric methylene stretching modes at 2889 cm^{-1} and N−CH$_3$ at 3040 cm^{-1}. p-Polarized spectra were used only as part of the orientational and conformational analysis for identifying relative changes, not for establishing the adsorption models due to overall lower signal intensities inherent to this sampling geometry.

The reduced signal intensity of the collected signal in p-polarized spectra is a consequence of the TIR Raman sampling geometry where the Raman scattered signal collected along the x-axis (along the surface normal) is weak as compared to the scattering signals collected along the y-axis from the interaction of the oscillating molecular dipoles with the E_y electric field. The stronger signal of the antisymmetric vibrational modes in the p-polarized spectra implies stronger interaction of the off-diagonal Raman tensor elements with p-polarized incident light due to more favorable alignment of their oscillating dipoles and stronger interaction of these modes with the incident p-polarized electric field.[34,35,59,60]

The symmetric methylene stretching modes at 2852 cm^{-1} are clearly dominating the Raman spectrum of the surfactant molecule in the C−H region, with high Raman scattering cross sections for the C−H stretching modes, in particular the symmetric vibrational modes (Table 1). The CH$_3$-symmetric stretching mode at 2872 cm^{-1} is barely visible in the presented Raman spectrum, although its intrinsic Raman scattering cross section is higher than that for the methylene group. However,
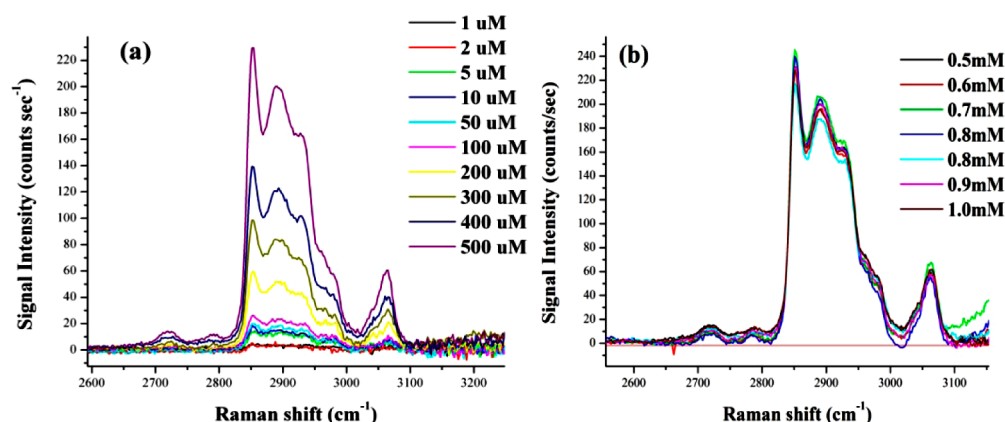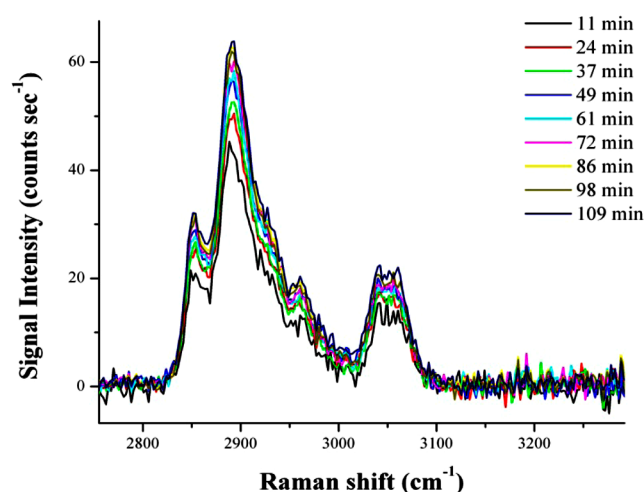
Figure 5. Spectral analysis and comparison of BDMHA$^+$ in the concentration range of (a) 0.001−0.5 mM and (b) 0.5−1.0 mM at adsorption equilibrium.

the number density of methylenes per molecule is 15 methylenes versus 1 methyl group in the hexadecyl chain, making them the main contributors to the C−H stretching signal. The antisymmetric modes of both the methylene groups and the methyl terminal group are clearly discernible at 2889 and 2965 cm^{-1}, respectively, although not well resolved. The signal at 2927 cm^{-1} is tentatively assigned to the Fermi resonance (ν_{FR}) of the symmetric methylene stretch; Fermi resonances, which are combinations of the overtones of fundamental C−H vibrational modes in the low-frequency region (around 1300−1460 cm^{-1}) and the C−H fundamental stretching modes in the high-frequency region of the same symmetry, are strongly represented in the high-frequency Raman spectrum[35] as well as the stretching vibrations from the benzyl ring at 3064 cm^{-1}.

Additional minor Raman vibrational modes show in the spectral region between 2700 and 3100 cm^{-1}. The weak peaks at 2718 and at 2789 cm^{-1} are assigned to the overtone of the fundamental C−H symmetric bending mode (scissoring or symmetric bend), and a combination band of the fundamental in-plane bending mode and the out-of-plane C−H deformations of the benzyl group.[61] Raman vibrational modes appear at 2980 cm^{-1} for the symmetric N−CH$_3$, and at 3040 cm^{-1} for its antisymmetric mode that shifts to lower wavenumber of 3038 cm^{-1} at lower concentrations. This N−CH$_3$ antisymmetric band was observed in a previous study of CTAB adsorption,[35] together with a second smaller peak at 3017 cm^{-1} that appeared to merge into one mode. They were identified as two independent and out-of-phase vibrational modes by a 2D simulation. In the spectral analysis of this study, both signals at 3017 and 3040 cm^{-1} increase proportional to surface coverage in s-polarized spectra, although the smaller peak at 3017 cm^{-1} is barely distinguishable from the baseline noise in some spectra and disappears in p-polarized spectra. Addition of magnesium chloride did not have any modifying effects on the Raman spectra when comparing pure surfactant spectra with spectra of surfactant with metal salt addition.

Structural Analysis of the Pure Surfactant. Structural analysis of the pure surfactant was carried out by using signal intensity ratios and potential ratio changes of the CH$_2$ antisymmetric/CH$_2$ symmetric stretching modes as well as CH$_2$/CH$_3$ modes (Figure 5, a and b) to identify any potential restructuring of the studied surfactant as a function of concentration. A second experiment evaluated the intensity ratio changes in p-polarized sampling geometry as function of

time at one single concentration (Figure 6), but neither revealed any changes in intensity ratios that might hint toward surfactant reorientation within the TIR probing depth.

Figure 6. Spectral analysis and comparison of BDMHA$^+$ (0.4 mM) in p-polarization mode. Signal intensity evolution as function of time.

Signal intensities in both s- and p-polarization and two different signal collection geometries provided the input to compare the signal intensity ratios: p-polarization in TIR geometry probes the symmetric α'_{xx} and the off-diagonal derived Raman tensors and is most sensitive toward vibrational modes with their oscillating dipoles at the surface aligned with the incident p-polarized electric field enhancing the scattering signals of the most susceptible antisymmetric vibrational stretching modes. p-Polarized incident light with no polarizer in the collection optics (defined as P$_{x+y}$) probes primarily the scattering intensity of the off-diagonal derived Raman tensor α'_{xz} (=α'_{yz} at the isotropic surface), and α'_{yx} (=α'_{xy}) along both the x-and y-axes;[62,63] Raman scattering from the α'_{zz} tensor that probes the vibrational modes along the surface are negligibly small in this sampling geometry; no polarizer was integrated in the collection optics, since the collected Raman scattering signals in p-polarized sampling geometry are weaker as compared to s-polarization mode signal collection and would be even more attenuated with selective filtering of the respective scattering modes.[34,35] s-Polarized incident light sampling geometry with the polarizer set to probe the

scattering intensity along the *y*-axis (S_y) probes primarily the symmetric derived Raman tensor α'_{yy} (=α'_{xx} at the isotropic surface), i.e., symmetric methylene stretching vibrations, with resulting strong Raman signal intensity. s-Polarized incident light without polarizer in the collection optics (S_{x+y}), which gave the strongest Raman scattering intensity, was the primary sampling geometry for all isotherm-related experiments.

Adsorption of Pure Benzyldimethylhexadecylammonium Chloride. Adsorption isotherms of the surfactant BDMHA$^+$ and adsorption models were based on the Raman scattering intensity of the symmetric methylene stretching mode as the primary indicator (Figures 7−9), and on the
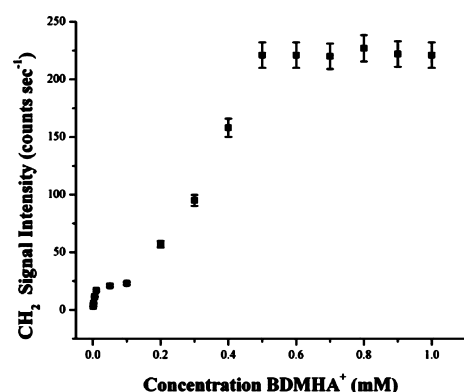

Figure 7. Adsorption isotherm of BDMHA$^+$ based on the CH$_2$ signal intensity − linear scale.
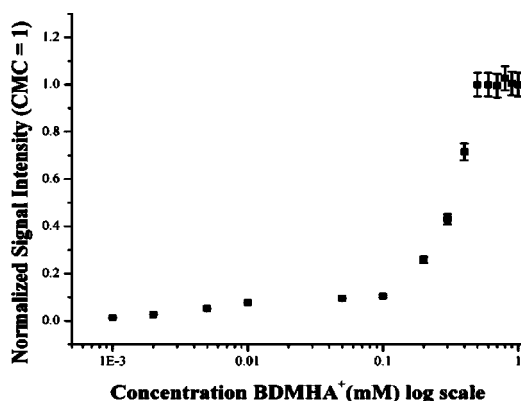

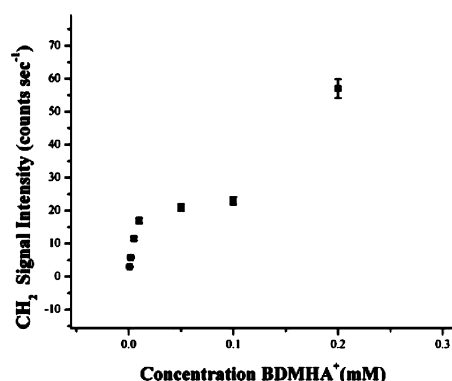**Figure 8.** Adsorption isotherm based on the normalized CH$_2$ signal intensity.

Figure 9. Exploded view the of C−H on the stretching region at low conc.

benzyl vibrational mode used as secondary and Supporting Information (Figure 10). The TIR Raman spectral analysis of
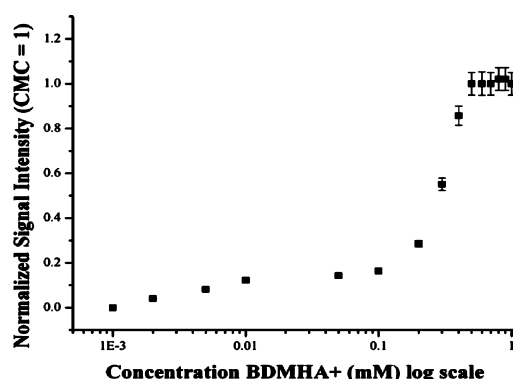

Figure 10. Adsorption isotherm based on the normalized benzyl signal intensity.

the respective concentrations (spectral overlays in Figure 5a,b) provided the input for establishing the isotherms as presented in Figures 7−10 on an absolute scale in counts s^{-1} and a normalized scale (cmc = 1). The baseline offset noticeable around 3000 cm^{-1} is the result of baseline fluctuations and was not considered a concern in terms of signal intensity interpretation.

The trends in the adsorption isotherms, based on the CH$_2$ symmetric stretching mode of the pure surfactant (Figures 7−10), are in agreement with the isotherm based on the signal intensity of the benzyl vibrational mode at 3064 cm^{-1} (Figure 9), in terms of dΓ/d log [C], cmc, and adsorption slopes, with some variability in the low-concentration region. The signal intensities observed at concentrations below the cmc and most likely above the cmc up to 1 mM originate from the molecules adsorbed at the surface with negligible contribution from the molecules in the bulk.[35] The spectral information that was obtained for surfactant concentrations from the detection limit of 1 μM (corresponding to a fractional coverage of 0.014 relative to the cmc = 1) to 1 mM of surfactant includes the concentration region below and above the cmc of 0.5 mM and appeared sufficient for determining the adsorption isotherm without the need to probe higher surfactant concentrations, since concentrations above 1 mM may contain nonnegligible bulk signal contributions that need to be factored out.

One significant difference in the adsorption behavior of BDMHA$^+$ as compared to CTAB and the related CTAC was the slow adsorption process, or slow adsorption kinetics,[35,42] that were noticeable throughout the concentration range studied, but most pronounced with the pure surfactant at concentrations right below and above the cmc. The slow adsorption process, with up to 6 h for the surfactant to reach equilibrium, might reflect the slow kinetics of aggregate formation and restructuring in solution.[64] The different head-group geometry containing the bulky benzyl group with a large surface area,[65] and considered equivalent to 3−3.5 additional methylene groups added to the hydrophobic portion,[66] increases the interfacial area with the surrounding water molecules and adds more hydrophobic character to the surfactant, which favors both micellization and adsorption but also poses mobility constraints due to its bulky head-group ligand. The benzyl ligand is part of the head-group function and head groups are not considered a part of the micellar core,[66]

with their energetically most favorable conformation suggested as lying parallel to the micellar outer surface.[65]

The observed slow adsorption kinetics, with a strong dependence on the time elapsed between sample preparation and the actual study in the Raman spectroscopic cell, were particularly evident for all surfactant concentrations around and above the cmc and, in particular, with samples that were kept overnight before testing. These samples did not reach the adsorption plateau until approximately 4−6 h, whereas freshly prepared samples attained their adsorption equilibrium within 3 h or less (Figure 11), at reproducible signal intensities of 221 counts s[−1].
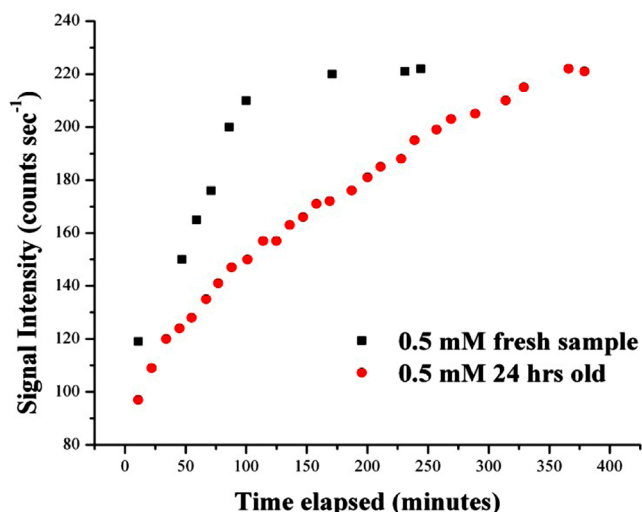

Figure 11. Adsorption kinetics for BDMHA[+] (0.5 mM) of a fresh sample versus 24 h old sample.

The slower than typical adsorption kinetics associated with the aged samples and also the generally slow adsorption process might be related to slow kinetics of aggregate formation and restructuring in solution, intensified by the intrinsic surface property itself that affects orientation, order, and surfactant−surface interactions, as suggested in the literature and in a current adsorption study of the same surfactant with faster adsorption kinetics at a hydrophobic silica surface under otherwise identical experimental conditions.[67−70]

Adsorption at the silica−water interface is initiated by electrostatic attraction between the negatively charged silica surface,[1,2] estimated as −0.013 C/m^{2} at neutral pH, and the positively charged ammonium head group; the initial onset of adsorption reaches an intermediate plateau region at 10 uM (Figures 7−9), followed by an almost linear slope with low adsorption coefficient or low slope of $d\Gamma/d \log C$ in the adsorption isotherm between 10 and 50 μM, with slight increase between 50 and 100 μM that changes abruptly to a higher and almost exponentially increasing adsorption slope arising from hydrophobic effects at the point of the critical surface aggregation concentration (csac),[42] until the equilibrium plateau with maximum surface coverage is reached at the cmc. The adsorption isotherms, with two distinct plateau regions, match the two-step adsorption model suggested by Atkin et al. and Somasundaran et al.,[1,71] in context with formation of spherical or quasi-spherical micelles. A clear breakpoint at an equilibrium concentration of approximately 0.5 mM forms the intersection between the increasing slope

before the cmc and the linear portion of the adsorption slope above the cmc, and is indicative of the cmc value of 0.50 mM that was obtained from curve fitting (Figure 12) and taking the point of intersection of the fitted slopes (detailed information in the Supporting Information).
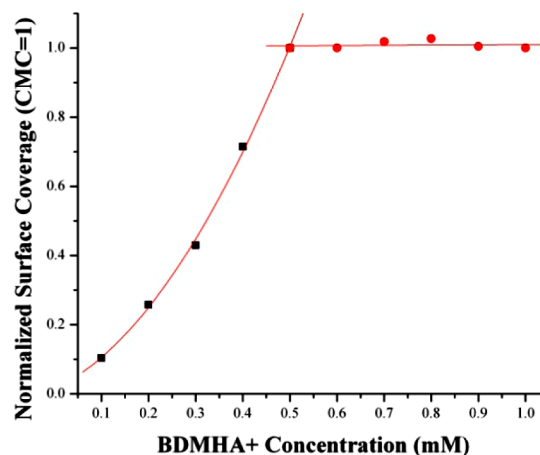

Figure 12. Adsorption isotherm curve fitting and cmc for pure BDMHA[+] normalized to cmc = 1.

Effects of Magnesium Chloride on Thermodynamic Properties of Surfactant Adsorption. The addition of 5 mM divalent metal salt, in this experiment magnesium chloride (as $MgCl_2 \cdot 6H_2O$), was already sufficient to modify both thermodynamic properties of the pure surfactant, i.e., free energy of micellization, cmc, surface coverage, and adsorption kinetics in all three distinct adsorption regions, i.e., at very low surfactant concentrations, where attraction to the surface is governed by electrostatic forces, in the hemimicelle formation region, and in the adsorption plateau region at surfactant concentrations above the cmc. The cmc of the surfactant shifted to 0.050 mM or 50 μM, accompanied by a higher adsorption slope $d\Gamma/d \log [conc]$ in the hemimicelle region (Figure 13b), relative to the pure surfactant. The maximum surface coverage decreased to one-half of the number density of the pure surfactant, or 0.51 normalized surface coverage, based on the measured maximum signal intensity of 112 counts s[−1] at the cmc, as compared to the pure surfactant, that corresponds to a Raman scattering intensity of 221 counts s[−1] at maximum coverage. Lower surface coverage, along with exponentially decreasing cmc (or linear on a log scale), points toward more favorable aggregation in solution, due to more efficient screening of the surfactant head group,[38] and concurrent change of the free energy of micellization. Restructuring and aggregation of the surfactant becomes more favorable with most likely increasing aggregation numbers in solution relative to the pure surfactant with N_{agg} (number of alkyl chains in the micelle) values estimated in the range of 90 (by fluorescence) and 102 (light scattering).[65] Similar effects of chloride-containing electrolyte have been observed in the adsorption isotherm of cetyltrimethylammonium chloride.[26] This information alone does not allow deducing the exact nature of the structures but gives hints toward more densely packed aggregates in solution that are energetically more favorable than the alternative energy lowering mechanism of adsorption.

The adsorption isotherm of the surfactant with low electrolyte addition shows three distinct regions, resembling
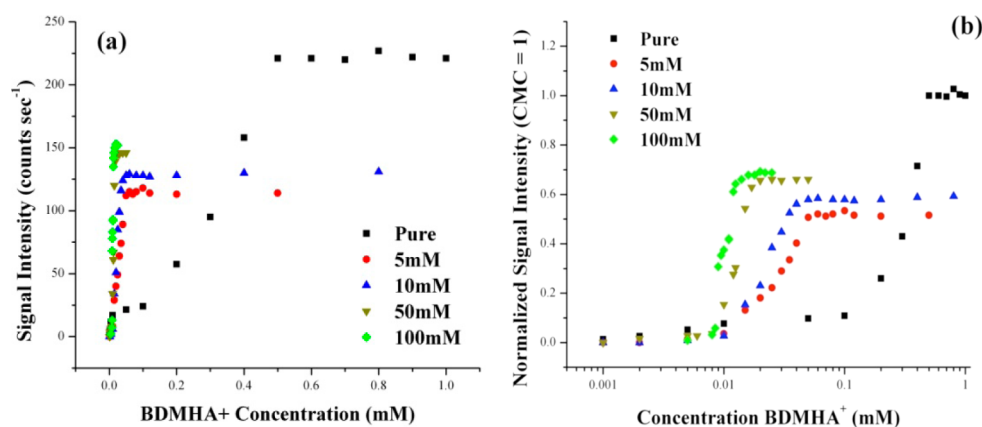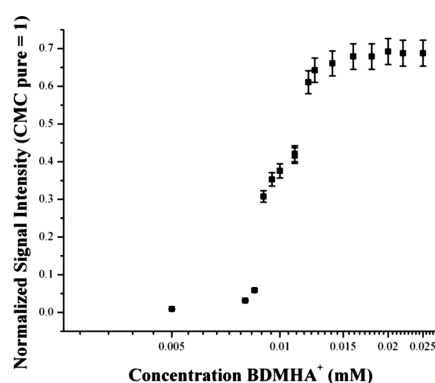
Figure 13. Adsorption isotherms of the pure surfactant (■); surfactant + 5 (●); + 10 (▲); + 50 (▼); and + 100 mM (◆) MgCl₂; error bars are omitted for clarity. (a) CH₂ intensity in counts s^{-1} vs concentration, linear scale. (b) Normalized signal intensity vs concentration, log scale.

vaguely the classic two-step adsorption isotherm models, as observed by Tyrode et al. and Woods et al. with the adsorption of cetyltrimethylammonium bromide (CTAB) on silica surfaces,[35,36] and by Somasundaran et al. with the adsorption isotherms of nonionic and anionic surfactants on alumina surfaces,[2] with some deviation in the low-concentration region of the adsorption isotherm. The lower adsorption plateau region at concentrations below 5 μM is missing in the isotherm, as indicated by the absence of Raman signals in this concentration region that is not related to loss of signal sensitivity. The electrostatically driven adsorption mechanism is not available upon addition of magnesium salt to the solution at surfactant concentrations from 1 to 5 μM. At higher surfactant concentrations, above 5 μM, at the onset of the critical surface aggregate concentration (csac),[1] surfactant adsorption is promoted by the hydrophobic effect, and reaches equilibrium conditions at the cmc, when both solution and surface aggregates have reached their optimum lowest energy states in solution and the silica surface.[38]

Addition of 10, 50, and 100 mM of MgCl₂ leads to further cmc reduction to 0.042, 0.018, and 0.014 mM, respectively, as estimated from the plot and curve fitting (Figure 13); interestingly, an increasing trend of the normalized surface coverage to 0.59, 0.66, and 0.69 is observed for the surfactant containing 10, 50, and 100 mM of metal salt (Table 2), respectively, with high adsorption slopes (dΓ/d log [conc]) that represent the hemimicelle aggregation region (Figure 13, a and b). The lower plateau region in the adsorption isotherm of the surfactant with 50 mM electrolyte concentration reappears again at a concentration of 2 μM, and also for the surfactant with 100 mM of electrolyte addition at 5 μM (although at the analytical detection limit). This suggests that hydrophobic effects are already present at these low concentrations, since adsorption due to electrostatic attraction is unlikely.

The isotherm of the surfactant with the high metal salt concentration of 100 mM reveals unusual, nonlinear behavior in the center portion of the adsorption slope as compared to the remaining isotherms. The critical experiments were duplicated using two independent surfactant mixtures to confirm the validity of the isotherm in the aggregate formation region that exhibits a breakpoint in the usually linear adsorption slope (Figure 14) comparable to a four-step adsorption model, as proposed by several authors for certain types of surfactant−interface interactions and aggregate restructuring.[2,37,42,64]

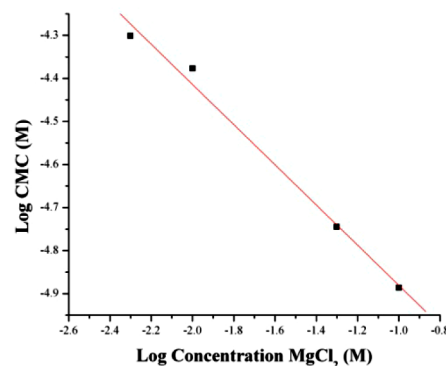**Figure 14.** Adsorption isotherm of the surfactant + 100 mM MgCl₂; normalized intensity, log scale.

The cmc values decrease exponentially according to the cmc versus electrolyte relationship for ionic surfactants:[72]

$$\log cmc = a - b \log[C] \tag{6}$$

or

$$cmc = [C]e^{a-b} \tag{7}$$

where a and b are surface property and electrolyte−surfactant specific constants and $[C]$ represents the electrolyte concentration. The value obtained for $b = -0.45$ ($R^2 = 0.995$) from the curve-fitting coefficient (Figure 15) lies below the expected range of -0.6 to -1.2 reported in the literature for common

Figure 15. Correlation of cmc vs electrolyte concentration for BDMHA⁺−MgCl₂.

Table 2. Adsorption Energy Parameters from Adsorption Isotherm Fitting

surfactant system	$\Delta\Delta G^{\circ}_{ads}$ (kJ mol^{-1})	K_{mod}	K_{mod} R^2	g	K_L	cmc (μM)	Γ_{max} cmc = 1
pure surfactant	-19 ± 3	$1.4 \times 10^5 \pm 1.400$	0.998	N.A.	K_{mod}	500 ± 5	1.00
surfactant + 5 mM MgCl$_2$	-25 ± 2	$1.4 \times 10^6 \pm 2 \times 10^4$	0.998	0.5	$K_{mod}\,e^{-0.5\theta}$	50 ± 0.5	0.51
surfactant + 10 mM MgCl$_2$	-39 ± 8	$4.2 \times 10^8 \pm 5.8 \times 10^6$	0.990	2.5	$K_{mod}\,e^{-2.5\theta}$	42 ± 0.5	0.59
surfactant + 50 mM MgCl$_2$	-44 ± 8	$2.6 \times 10^9 \pm 56.6 \times 10^6$	0.991	3	$K_{mod}\,e^{-3.0\theta}$	18 ± 0.5	0.66
surfactant + 100 mM MgCl$_2$	-42 ± 1	$1.9 \times 10^9 \pm 2.7 \times 10^7$	0.998	2.5	$K_{mod}\,e^{-2.5\theta}$	14 ± 0.4	0.69
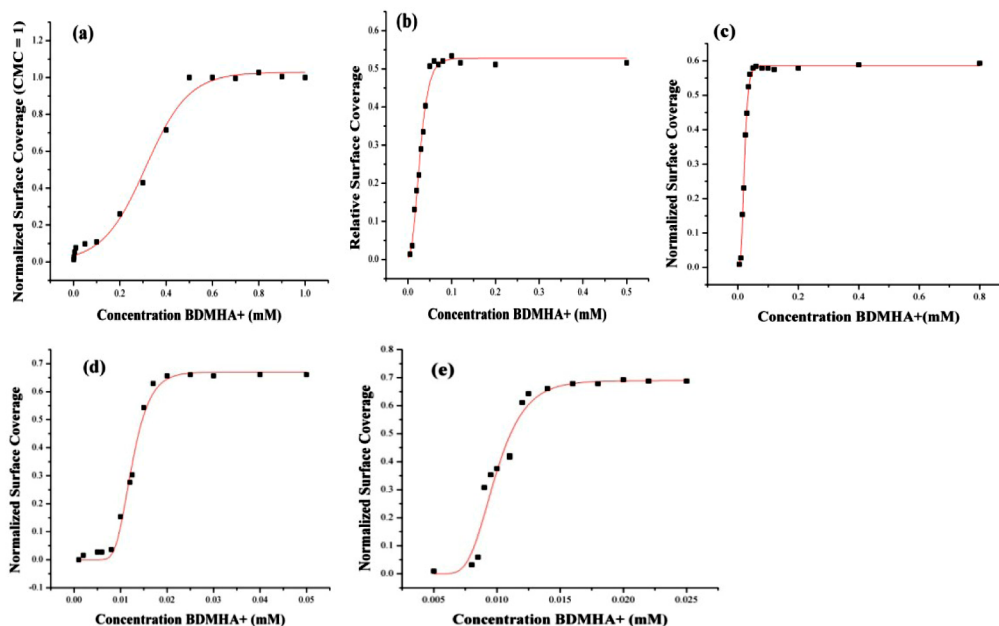
Figure 16. Adsorption isotherm fitted to the FFG adsorption model using sigmoidal fitting models: (a) pure surfactant, (b) surfactant + 5 mM MgCl$_2$, (c) surfactant + 10 mM MgCl$_2$, (d) surfactant + 50 mM MgCl$_2$, and (e) surfactant + 100 mM MgCl$_2$.

surfactant−electrolyte systems, implying less effective screening of the head-group function in BDMHA$^+$ by the magnesium salt.

The adsorption isotherms were fitted to a Langmuir or modified Langmuir isotherm; K_{mod} was determined from the intercept of the linearized logarithmic expression as shown in eq 8 and referenced to the molarity of water of 55.5 mol (Table 2). The expression for the modified Langmuir isotherm in eq 3 was rearranged to give the linearized logarithmic expression:

$$\ln\left(\frac{\theta}{1-\theta}\right) - g\theta = \ln K_{mod} + \ln[C] \qquad (8)$$

The measured values for the equilibrium constant were determined by plotting $\ln(\theta/(1-\theta) - g\theta)$ versus $\ln[C]$ and varying the parameter g to obtain the best linear fit correlation and determine the best fit g parameter and the modified adsorption constant from the intercept. The fitted isotherms and computed adsorption equilibrium for the pure surfactant showed a change of the Gibbs free energy of adsorption of -19 (±3) kJ/mol. The free energy of micellization (ΔG°_{mic}) is reported as -43 kJ/mol in the literature for the pure surfactant,[54] and no attempt was made to determine it from the current data. The association or dissociation parameter α, which describes the ratio of bound versus dissociated counterions relative to the number of surfactant molecules in the micellar aggregates, needs to be determined by a separate technique, i.e., conductivity measurement.[73] A calculation based on literature values is not informative, since the α value has been listed in the literature as varying between 0.22, 0.40,[65] and

0.49,[39,54] depending on the methods that were used, and would not apply to the surfactant with addition of the metal salt.

The Langmuir adsorption constant determined from the fitted data for the pure surfactant does not indicate any specific deviation from a typical Langmuir adsorption model and no interaction energy parameter was defined for the isotherm of the pure surfactant showing actually two plateau regions. The interaction energy parameter for the surfactant with small addition of the magnesium salt shows only a small value of 0.5, whereas higher metal salt additions of 10 and 50 mM gave a g value of 2.5 and 3.0; the interaction parameter for the highest metal salt concentration did decrease to 2.5, showing a downward trend as reflected in the equilibrium adsorption constant, and also observed in other studies with high electrolyte concentrations.[43] The generally increasing interaction energy apparently arises from the high electrolyte concentrations providing the conditions for higher aggregation numbers and denser packing of the surfactant in solution and at the surface.

The change in the Gibbs free energy of adsorption is -19 (±3) kJ/mol for the pure surfactant, which decreased to -25 (±2) kJ/mol for the surfactant +5 mM magnesium salt, and to -39 (±8) kJ/mol for surfactant +10 mM of metal salt additive, reaching its minimum for the surfactant with a metal salt addition of 50 mM that showed the most favorable reduction of the free energy of adsorption at -44 (±8) kJ/mol. The change in the Gibbs free energy of adsorption of the surfactant with 100 mM of magnesium salt increased again to -42 (±1) kJ/mol (Table 2), consistent with a decrease of the interaction
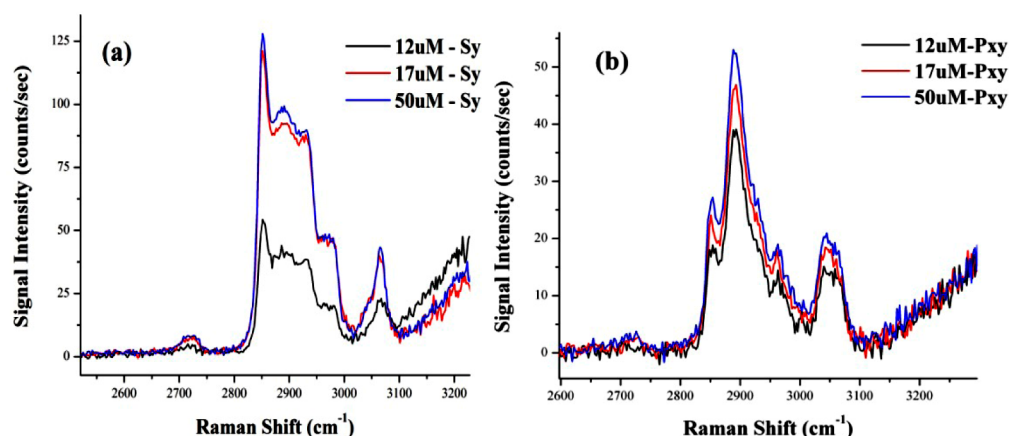
Figure 17. Spectral analysis and comparison of representative spectra acquired at 12 μM, 17 μM, and 50 μM concentrations of the surfactant with 50 mM MgCl$_2$ in (a) s-polarized and (b) p-polarized geometry.

parameter, and a trend reversal of the adsorption behavior at high electrolyte concentrations.

The isotherms of all five systems studied were curve fitted to the respective Langmuir or modified Langmuir model (Figure 16). The adsorption constants, K_{mod}, presented in Table 2, increase proportional to the metal salt added with the exception of the surfactant with 100 mM of magnesium salt, which shows an adsorption trend reversal. However, the adsorption slope with an additional step or intermediate plateau does not allow for a good correlation over the entire adsorption region and is based on the upper segment of the adsorption slope. The values for the observed equilibrium constant K_{mod} are valid under the assumption that the electrolyte activity coefficient is equal to unity and corrections would be negligible at these small concentration if no further interactions between the species in solution are involved; there might be a slight bias in these values, since some interferences might be expected with ionic surfactants.[72]

Structural Analysis of Surfactant with High Electrolyte Concentration. More detailed orientational analysis of p- and s-polarized spectra and comparison of intensity ratio changes of the CH$_2$ and antisymmetric CH$_3$ vibrational modes was carried out by repeating one of the adsorption isotherm studies, namely the surfactant with 50 mM of metal salt addition, in s-polarized sampling geometry with a polarizer integrated in the light collection optics for collecting scattering intensities along the y-axis (S$_y$), and duplicating three of the surfactant concentrations, 12, 17, and 50 μM in p-polarized geometry (P$_{x+y}$). The three surfactant concentrations chosen represent the critical concentrations at the onset of aggregate formation, before the cmc, and in the adsorption equilibrium (plateau) region above the cmc (Figure 17). Since absolute signal intensities of the vibrational modes detected in TIR Raman are related to the concentrations, they would not convey any structural information; structural changes may, however, be inferred from trends in the signal intensity ratios.

Overlaid spectra of the set in p- and s-polarized modes (Figures 17, a and b) show a slight decrease in intensity ratio of the antisymmetric CH$_3$ stretch versus the symmetric CH$_2$ stretching mode in the p-polarized spectra when going from the lowest surfactant concentration of 12 to 50 μM (Table 3). An unambiguous interpretation in terms of increased structural ordering, or conformational transitions, however, is not possible, since the decreasing trend of the signal intensity

**Table 3. Vibrational Mode Intensity Ratios from p- and s-Polarized Spectra of Surfactant with 50 mM of MgCl$_2$**

	concentration of surfactant		
	12 μM	17 μM	50 μM
S$_y$/S$_y$ ratio			
CH$_3$ ν_{as}/CH$_2$ ν_s	0.41 ± 0.03	0.41 ± 0.02	0.39 ± 0.01
P$_{xy}$/P$_{xy}$ ratio			
CH$_3$ ν_{as}/CH$_2$ ν_s	0.78 ± 0.15	0.74 ± 0.12	0.69 ± 0.10
CH$_2$ ν_{as}/CH$_2$ ν_s	2.01 ± 0.21	1.96 ± 0.20	1.92 ± 0.17
P$_{xy}$/S$_y$ ratio			
CH$_3$ ν_{as}/CH$_3$ ν_{as}	0.63 ± 0.11	0.43 ± 0.05	0.36 ± 0.04
CH$_2$ ν_{as}/CH$_2$ ν_{as}	0.85 ± 0.10	0.58 ± 0.03	0.52 ± 0.02
CH$_2$ ν_s/CH$_2$ ν_s	0.33 ± 0.04	0.23 ± 0.0.02	0.20 ± 0.02

ratio is not confirmed within the set of s-polarized spectra. No shift of the Raman peak positions to lower frequency occurred[60,74] that would be characteristic of a transition from less ordered molecular surface structures with gauche defects in the alkyl chains to a more crystalline-like ordered configuration.[75,76] The negligible shifts in frequency or peak positions observed with the prominent vibrational modes, however, are much smaller than those reported in literature for a typical transition to a more ordered arrangement (Table 4).[60,76]

Table 4. Frequency Shift Observed in the Concentration Range of 12−50 μM

Δ (cm^{-1})	P$_{xy}$	S$_y$
CH$_2$ ν_s	−1.5	+0.5
CH$_2$ ν_{as}	−1.8	+4.0
CH$_3$ ν_{as}	−2.0	−1.0

Effects of Background Solution on the Water Structure. The Raman spectral baseline that usually exhibits a straight line with the water background signal corrected showed a positive offset of the water band in the frequency region of 3300−3400 cm^{-1} that increased reproducibly and proportional to the increase in magnesium chloride concentration, but was independent of the surfactant concentration (Figure 18). This offset water signal cannot have its origin in the surfactant adsorption, since no water signal deviation was observed in experimental work that involved the pure surfactant. It typically indicates a change at the silica−water
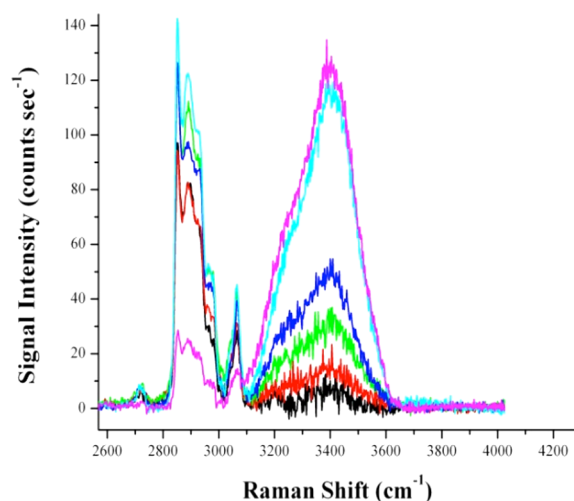
Figure 18. Offset water signal as function of magnesium ion concentration: pure surfactant (black line); surfactant + 5 mM Mg^{2+} (red line); surfactant + 10 mM Mg^{2+} (green line); surfactant + 50 mM Mg^{2+} (dark blue line); 0.014 mM surfactant + 100 mM Mg^{2+} (light blue line); 0.010 mM surfactant + 100 mM Mg^{2+} (pink line).

interface relative to the background signal obtained from a pure silica−water interface, and, in this experimental setup, a change in the water structure within the electrical double layer and the bulk that corresponds to the probing depth of the evanescent field of 100 nm, due to the water structure modifying properties of magnesium chloride.

The spectral analysis reproducibly shows an increase of the vibrational band (peak maximum at 3400 cm^{-1}) that corresponds to the less symmetric and less ordered waterlike structure,[77] with a significant attenuation of the more symmetric, icelike band (at 3200 cm^{-1}) in s-polarized geometry. The unusual reduction of the icelike vibrational bands emphasizes the magnesium ion's water-structure-breaking property that causes reorientation of the water molecules in the electrical double layer at the interface and in the bulk to a less H-bonded water structure with higher susceptibility of the water molecule's off-diagonal Raman tensor to the incident p-polarized electric field. These phenomena at the silica−water interface have previously been reported in context with divalent metal ion effects, showing water signal attenuating effects for magnesium ion at the silica−water interface at neutral pH conditions, with enhancement of the liquidlike low-symmetry vibrational band.[78−81]

IR and Raman spectroscopic studies by Allen et al. of the symmetric versus asymmetric vibrational water signal intensities as function of metal salt addition in the bulk aqueous solution found a similar decline of the icelike water vibrational signal as response to metal salt addition in the bulk solution,[82] from the solvation of both cationic and anionic species and their H-bonding disrupting properties.[83,84] Studies using X-ray absorption spectroscopy (XAS) for specifically studying the anion function, confirm that the anionic halide ions contribute to the water structure distortion,[85] as much as other anionic species of relatively small size, i.e., nitrates, that according to early research studies affect the liquidlike band at 3400 cm^{-1}.[83,86] These findings would agree with the TIR Raman spectra that show no significant deviation of the pure water background signal (neat water) versus the signal with surfactant added containing only low ion concentrations versus the addition of magnesium chloride in the concentration range of

5−100 mM, where both cation and anions exceed by far the surfactant concentrations, and both contribute to ionic species in solution.

CONCLUSION

The study was able to elucidate the details of adsorption behavior of the surfactant $BDMHA^+$ by taking advantage of long acquisition times and strong incident excitation power to enhance the first derivative of the signal versus time gradient that emphasizes the slow adsorption kinetics and adsorption isotherm of the pure surfactant at the silica−water interface, and change of adsorption behavior induced by metal salt addition. The study is consistent with previous findings that conformational order or restructuring of the surfactant molecules in the hemimicelle and monolayer forming regions is not significant for the pure surfactant, although there are some indicators that the most likely structure is a spherical or elongated globular aggregate with optimum packing of the monomers for minimization of the free energy of adsorption.

In the presence of metal salt, the structure may evolve into more densely packed aggregates at the silica−water surface due to more efficient screening of head-group charges and increased hydrophobic effects that are offset by opposing mechanisms when the salt content is increased above 50 mM. This study further confirmed literature values regarding the typical thermodynamic properties, i.e., cmc lowering and surface coverage increase, proportional to electrolyte addition, and effective enhancement of these properties at low electrolyte concentrations that minimize the amount of the chemical requirement.

Modulation of the intrinsic surface coverage by addition of low concentrations of a divalent metal salt, as demonstrated in this study, and controllable surface coverage at low surfactant concentrations in the presence of moderate divalent metal salt concentrations, makes this type of surfactant attractive in industrial and environmental applications where efficient surfactant treatments at low operating costs and minimum adverse effects on the environment are desirable.

ASSOCIATED CONTENT

⑤ Supporting Information

The Supporting Information contains detailed description of the evanescent electric field enhancement at the silica−water interface for p- and s-polarized incident light in TIR Raman sampling geometry, adsorption isotherm analysis of the pure surfactant, and curve-fitting process for cmc determination. This material is available free of charge via the Internet at http://pubs.acs.org.

AUTHOR INFORMATION

Corresponding Author
*E-mail: sbaldelli@uh.edu.

Notes

The authors declare no competing financial interest.

ACKNOWLEDGMENTS

■ REFERENCES

(1) Atkin, R.; Craig, V. S. J.; Wanless, E. J.; Biggs, S. *Adv. Colloid Interface Sci.* **2003**, *103*, 219−304.

(2) Somasundaran, P.; Huang, U. L. *Adv. Colloid Interface Sci.* **2000**, *88*, 179−208.

(3) Lunkenheimer, K.; Lind, A.; Jost, M. *J. Phys. Chem. B* **2003**, *107*, 7527−7531.

(4) Farías, T.; Ménorval, L. C. d.; Zajac, J.; Rivera, A. *Colloids Surf., A* **2009**, *345*, 51−57.

(5) Gonzalez-Perez, A.; Castillo, J. L. d.; Czapkiewicz, J.; Rodríguez, J. R. *J. Phys. Chem. B* **2001**, *105*, 1720−1724.

(6) Gonzalez-Perez, A.; Czapkiewicz, J.; Prieto, G.; Rodríguez, J. R. *Colloid Polym. Sci.* **2003**, *281*, 1191−1195.

(7) Trompette, J. L.; Zajac, J.; Keh, E.; Partyka, S. *Langmuir* **1994**, *10*, 812−818.

(8) Avranas, A.; Malasidou, E.; Mandrazidou, I. *J. Colloid Interface Sci.* **1998**, *207*, 363−370.

(9) Gonzalez-Perez, A.; Castillo, J. L. D.; Czapkiewicz, J.; Rodrıguez, J. R. *Colloid Polym. Sci.* **2002**, *280*, 503−508.

(10) Gonzalez-Perez, A.; Czapkiewicz, J.; Castillo, J. L. D.; Rodríguez, J. R. *Colloids Surf., A* **2001**, *193*, 129−137.

(11) Migahed, M. A.; AL-Sabag, A. M. *Chem. Eng. Commun.* **2009**, *196*, 1054−1075.

(12) Umoren, S. A.; Ebenso, E. E.; Okafor, P. C.; Ogbobe, O. *Pigment Resin Technol.* **2006**, *35/6*, 346−352.

(13) Zanten, R. v. *SPE No. 1414474* **2011**.

(14) Ke, M.; Stevens, R. F.; Qu, Q. NACE paper # 08630, presented at NACE, New Orleans, March 16−20, 2008.

(15) Somasundaran, P.; Zhang, L. *J. Pet. Sci. Eng.* **2006**, *52*, 198−212.

(16) Adibhatla, B.; Mohanty, K. K.; Berger, P.; Lee, C. *J. Pet. Sci. Eng.* **2006**, *52*, 227−236.

(17) Thibaut, A.; Misselyn-Bauduin, A.; Grandjean, J.; Broze, G.; Jerome, R. *Langmuir* **2000**, *16*, 9192−9198.

(18) Ball, B.; Fuerstenau, D. W. **1971**, 361-371.

(19) Fainerman, V. B.; Miller, R.; Mohwald, H. *J. Phys. Chem. B* **2002**, *106*, 809−819.

(20) Tomson, M. B.; Kan, A. T.; Fu, G.; Shen, D.; Nasr-El-Din, H. A. *SPE Journal, # 100494* **2009**, 325−336.

(21) Ismail, Z. Z.; Tezel, U.; Pavlostathis, S. G. *Water Res.* **2010**, *44*, 2303−2313.

(22) Rodriguez-Navarro, C.; Doehne, E.; Sebastian, E. *Langmuir* **2000**, *16*, 947−854.

(23) Stubenrauch, C.; Khristov, K. *J. Colloid Interface Sci.* **2005**, *286*, 710−718.

(24) Elliot, J.; Cook, R. NACE paper # 08213, presented at NACE, New Orleans, March 16−20, 2008.

(25) Besteman, K.; Zevenbergen, M. A. G.; Lemay, S. G. *Phys. Rev. E* **2005**, *72*, 061501.

(26) Atkin, R.; Craig, V. S. J.; Wanless, E. J.; Biggs, S. *J. Colloid Interface Sci.* **2003**, *266*, 236−244.

(27) Butt, H.-J.; Graf, K.; Kappl, M. In *Physics and Chemistry of Interfaces*, 2nd ed. (4th reprint); Wiley Publishing: Weinheim, Germany, 2011; Chapter 9, pp 198−201.

(28) Greene, P. R.; Bain, C. D. *Colloids Surf., B* **2005**, *45*, 174−180.

(29) Lee, C.; Bain, C. D. *Biochim. Biophys. Acta* **2005**, *1711*, 59−71.

(30) Beattie, D. A.; Fraenkel, R.; Winget, S. A.; Petersen, A.; Bain, C. D. *J. Phys. Chem. B* **2006**, *110*, 2278−2292.

(31) Okamura, E.; Umemura, J.; Takenaka, T. *J. Raman Spectrosc.* **1991**, *22*, 759−762.

(32) McKee, K. J.; Smith, E. A. *Rev. Sci. Instrum.* **2010**, *81*, 043106.

(33) Greene, P. R. Ph.D. Thesis, University of Oxford, Oxford, UK, 2003.

(34) Woods, D. A.; Bain, C. D. *Analyst* **2012**, *137*, 35−48.

(35) Tyrode, E.; Rutland, M. W.; Bain, C. D. *J. Am. Chem. Soc.* **2008**, *51*, 17434−17445.

(36) Woods, D. A.; Petkov, J.; Bain, C. D. *J. Phys. Chem. B* **2011**, *115*, 7341−7352.

(37) Fuerstenau, D. W. *Chem. Biosurf.* **1971**, *1*, 143−176.

(38) Nagarajan, R.; Ruckenstein, E. *Langmuir* **1991**, *7*, 2934−2969.

(39) Okano, L. T.; Quina, F. H.; Seoud, O. A. E. *Langmuir* **2000**, *16*, 3119−3123.

(40) Gonzalez-Perez, A.; Czapkiewicz, J.; Castillo, J. L. D.; Rodrıguez, J. R. *Colloids Surf., A* **2001**, *193*, 129−137.

(41) Dar, A. A.; Rather, G. M.; Das, A. R. *J. Phys. Chem. B* **2007**, *111*, 3122−3132.

(42) Atkin, R.; Craig, V. S. J.; Biggs, S. *Langmuir 2000* **2000**, *16*, 9374−9380.

(43) Hayes, P. L.; Chen, E. H.; Achtyl, J. L.; Geiger, F. M. *J. Phys. Chem. A* **2009**, *113*, 4269−4280.

(44) Novotny, L.; Hecht, B. *Principles of Nano-Optics*; Cambridge University Press: Cambridge, UK, 2008; reprint.

(45) Izgorodina, E. I.; Forsyth, M.; MacFarlane, D. R. *Phys. Chem. Chem. Phys.* **2009**, *11*, 2452−2458.

(46) Butt, H.-J.; Graf, K.; Kappl, M. *Physics and Chemistry of Interfaces*, 2nd ed. (4th reprint); Wiley Publishing: Weinheim, Germany, 2011.

(47) Norde, W. *Colloids and Interfaces in Life Sciences and Bionanotechnology*; CRC Press, Taylor & Francis Group: Boca Raton, FL, 2011.

(48) Petersen, P. B.; Saykally, R. J. *J. Phys. Chem. B* **2006**, *110*, 14060−140.

(49) Holland, J. G.; Jordan, D. S.; Geiger, F. M. *J. Phys. Chem. B* **2011**, *115*, 8338−8345; **2011**, *115*, 8338−8345.

(50) Malin, J. N.; Holland, J. G.; Geiger, F. M. *J. Phys. Chem. C* **2009**, *113*, 17795−17802; **2009**, *113*, 17795−17802.

(51) Dove, P. M.; Craven, C. M. *Geochim. Cosmochim. Acta* **2005**, *69*, 4963−4970.

(52) Strom, C.; Jonsson, B.; Soderman, O.; Hansson, P. *Colloids Surf., A* **1999**, *159*, 109−120 1999, 159, 109−120..

(53) Ledbetter, J. W.; Bowen, J. R. *Anal. Chem.* **1969**, *10*, 1345.

(54) Gonzalez-Perez, A.; Czapkiewicz, J.; Castillo, J. L. D.; Rodríguez, J. R. *Colloids Surf., A* **2001**, *193*, 129−137.

(55) Fuchs-Godec, R. *Colloids Surf., A* **2006**, *280*, 130−139.

(56) Aliaga, C.; Baldelli, S. *J. Phys. Chem. C* **2008**, *112*, 3064−3072.

(57) Santos, C. S.; Baldelli, S. *J. Phys. Chem. B* **2007**, *111*, 4715−4723.

(58) Santos, C. S.; Baldelli, S. *J. Phys. Chem. C* **2008**, *112*, 11459−11467.

(59) Long, D. A. *Raman Spectroscopy*; McGraw-Hill: New York, 1976; 47−71

(60) Orendorff, C. J.; Michael, W.; Ducey, J.; Pemberton, J. E. *J. Phys. Chem. A* **2002**, *106*, 6991−6998.

(61) Sears, W. M.; Hunt, J. L.; Stevens, J. R. *J. Chem. Phys.* **1982**, *77*.

(62) Iwamoto, R.; Miya, M.; Ohta, K.; Mima, S. *J. Am. Chem. Soc.* **1980**, 1212.

(63) Yamamoto, S.; Watarai, H. *J. Phys. Chem. C* **2008**, *112*, 12417−12424.

(64) Atkin, R.; Craig, V. S. J.; Biggs, S. *Langmuir* **2001**, *17*, 6155−6163.

(65) Okano, L. T.; Quina, F. H.; Seoud, O. A. E. *Langmuir* **2000**, *17*, 3119−3123.

(66) Treiner, C.; Makayssi, A. *Langmuir* **1992**, *8*, 794−800.

(67) Kumar, N.; Garoff, S.; Tilton, R. D. *Langmuir* **2004**, *20*, 4446−4451.

(68) York, R. L.; Mermut, O.; Phillips, D. C.; McCrea, K. R.; Ward, R. S.; Somorjai, G. A. *J. Phys. Chem. C* **2007**, *111*, 8866−8871.

(69) Li, P. X.; Dong, C. C.; Thomas, R. K. *Langmuir* **2011**, *27*, 1844−1852.

(70) Kiraly, Z.; Findenegg, G. H. *J. Phys. Chem. B* **1998**, *102*, 1203−1211.

(71) Somasundaran, P.; Fuerstenau, D. W. *J. Phys. Chem.* **1966**, *70*, 90.

(72) Hunter, R. J. *Foundations of Colloid Science*; Clarendon Press: Oxford, UK, 1987; Vol. *1*, Chapter 10.

(73) Zana, R. *Langmuir* **1996**, *12*, 1208−1211.

(74) Pemberton, J. E.; Mark, A.; Bryant, R.; Sobocinski, L.; Joa, S. L. *J. Phys. Chem.* **1992**, *96*, 3716−3182.

(75) Orendorff, C. J.; Michael, W.; Ducey, J.; Pemberton, J. E. *Anal. Chem.* **2003**, *75*, 3360−3368.

(76) Calkins, J. A.; Peacock, A. C.; Sazio, P. J. A; Allara, D. L.; Badding, J. V. *Langmuir* **2011**, *27*, 630−636.

(77) Kim, J.; Cremer, P. S. *J. Am. Chem. Soc.* **2000**, *122*, 12371−12372.

(78) Flores, S. C.; Kherb, J.; Konelick, N.; Chen, X.; Cremer, P. S. *J. Phys. Chem. C* **2012**, *116*, 5730−5734.

(79) Miranda, P. B.; Shen, Y. R. *J. Phys. Chem. B* **1999**, *103*, 3292−3307.

(80) Richmond, G. L. *Chem. Rev.* **2002**, *102*, 2693−2724.

(81) Shen, Y. R.; Ostroverkhov, V. *Chem. Rev.* **2006**, *106*, 1140−1154.

(82) Xu, M.; Spinney, R.; Allen, H. C. *J. Phys. Chem. B* **2009**, *113*, 4102−4110.

(83) Irish, D. E.; Davis, A. R. *Can. J. Chem.* **1968**, *46*, 943.

(84) Zhang, Y.-H.; Chan, C. K. *J. Phys. Chem. A* **2003**, *107*, 5956−5962.

(85) Cappa, C. D.; Smith, J. D.; Wilson, K. R.; Messer, B. M.; Gilles, M. K.; Cohen, R. C.; Saykally, R. J. *J. Phys. Chem. B* **2005**, *109*, 7046−7052.

(86) Irish, D. E.; Chang, T. G.; Tang, S.-Y. *J. Phys. Chem. B* **1981**, *85*, 1686−1692.